Journal of Applied Physics

Hydrogen incorporation into amorphous indium gallium zinc oxide thin-film transistors

Cite as: J. Appl. Phys. **131**, 105701 (2022); https://doi.org/10.1063/5.0078805
Submitted: 15 November 2021 • Accepted: 17 February 2022 • Published Online: 08 March 2022

George W. Mattson, Kyle T. Vogt, John F. Wager, et al.

COLLECTIONS

Paper published as part of the special topic on Defects in Semiconductors 2022

View Online
Export Citation
CrossMark

ARTICLES YOU MAY BE INTERESTED IN

Mist chemical vapor deposition of $Al_{1-x}Ti_xO_y$ thin films and their application to a high dielectric material
Journal of Applied Physics **131**, 105301 (2022); https://doi.org/10.1063/5.0073719

Breakdown characteristics of deep-ultraviolet $Al_{0.6}Ga_{0.4}N$ p-i-n avalanche photodiodes
Journal of Applied Physics **131**, 103102 (2022); https://doi.org/10.1063/5.0073515

Efficient defect control of zinc vacancy in undoped ZnO microtubes for optoelectronic applications
Journal of Applied Physics **131**, 105105 (2022); https://doi.org/10.1063/5.0077884

Journal of Applied Physics ARTICLE scitation.org/journal/jap

Hydrogen incorporation into amorphous indium gallium zinc oxide thin-film transistors

Cite as: J. Appl. Phys. **131**, 105701 (2022); doi: 10.1063/5.0078805
Submitted: 15 November 2021 · Accepted: 17 February 2022 ·
Published Online: 8 March 2022

George W. Mattson,[1] Kyle T. Vogt,[1] John F. Wager,[2] and Matt W. Graham[1,a)]

AFFILIATIONS

[1] Department of Physics, Oregon State University, Corvallis, Oregon 97331-6507, USA
[2] School of EECS, Oregon State University, Corvallis, Oregon 97331-5501, USA

Note: This paper is part of the Special Topic on Defects in Semiconductors.

[a)] **Author to whom correspondence should be addressed:** graham@physics.oregonstate.edu

ABSTRACT

An experimental study is conducted in which the subgap trap density of states (DoS) is measured by ultrabroadband photoconduction (UBPC) to examine hydrogen incorporation into the channel layer of top-gate amorphous indium gallium zinc oxide (a-IGZO) thin-film transistors (TFTs). UBPC reveals that hydrogen incorporation leads to the creation of a spectrally broad (∼0.3 eV FWHM) distribution of electronic states in the bandgap centered at 0.4 eV above the valence band mobility edge and to an increase in valence band tail state density. Concomitantly, drain current–gate voltage transfer curves demonstrate that hydrogen incorporation results in a negative shift in the turn-on voltage. Quantitatively, electronic state densities estimated by UBPC and the turn-on voltage shift are identical. These experimental findings imply that hydrogen acts as a donor in a-IGZO, but that its donor ionization energy is extraordinarily large, i.e., ∼2.8 eV, inconsistent with that of a normal donor. It is proposed that this anomalous donor behavior is a consequence of the negative-U property of hydrogen in a-IGZO in which hydrogen ionization precedes its incorporation into the lattice network.

I. INTRODUCTION

Amorphous indium gallium zinc oxide (a-IGZO) thin-film transistors (TFTs) constitute a well-established, maturing technology for the realization of commercial flat-panel display backplanes.[1–4] The performance of an a-IGZO TFT depends, to a large extent, on the subgap electronic state properties of the a-IGZO channel layer. Four primary types of intrinsic subgap states exist in a-IGZO, i.e., conduction band tail states (acceptor states exponentially distributed below the conduction band mobility edge), valence band tail states (donor states exponentially distributed above the valence band mobility edge), oxygen vacancy states (donor states forming a series of Gaussian-like peaks in the upper portion of the a-IGZO bandgap), and metal vacancy states (acceptor states giving Gaussian-like peaks in the lower portion of the a-IGZO bandgap).[5,6] Both types of band tail states and oxygen vacancy states are ubiquitous in a-IGZO, while ultrabroadband photoconduction (UBPC) assessment reveals that the concentration of metal vacancy states is quite variable, e.g., $\sim 10^{16}-10^{17}\,\mathrm{cm}^{-3}$ for the bottom-gate a-IGZO TFTs of Vogt *et al.*[5] and $\sim 2\times 10^{15}\,\mathrm{cm}^{-3}$ (see Table II) for the top-gate a-IGZO TFTs examined herein.

In addition to *intrinsic* subgap states, one type of *extrinsic* subgap state is commonly present in a-IGZO, i.e., hydrogen. Although there is abundant literature on the topic of hydrogen incorporation into a-IGZO,[7–21] this literature is confusing and often contradictory or even erroneous. The concept of hydrogen interacting with a-IGZO as a donor, contributing an electron to the conduction band, is well established through both computational[9,10,22] and experimental methods, the latter of which is confirmed by a negative shift in the TFT I_D-V_G transfer curve turn-on voltage (V_{ON}) after hydrogen incorporation.[11,16,23–29]

Hydrogen concentrations of order $10^{20}-10^{21}\,\mathrm{cm}^{-3}$ are often observed in a-IGZO via secondary ion mass spectrometry (SIMS) assessment[9]; however, this hydrogen must be predominantly electrically inactive, or the negative shifts in V_{ON} would be far larger. It is generally agreed that the donor behavior observed with hydrogen incorporation involves hydrogen bonding to oxygen in the disordered a-IGZO lattice, yielding OH^-.[9,22,29–31] Less firmly

TABLE I. Comparison of hydrogen concentration estimates from the four top-gate a-IGZO TFTs in Fig. 2. Estimates obtained from $I_D - V_G$ transfer curve shifts [Fig. 2(a)] are compared to measurements of the UBPC differential trap density taken at the valence band mobility edge or at −3.17 eV in Fig. 2(c) (*inset*). The Δ[H] column shows that the UBPC estimates give ∼30% excess hydrogen compared to $I_D - V_G$ estimates.

ΔV_{ON} (V)	$[H]_{ID-VG}$ (cm^{-3})	$[H]_{UBPC}$ (cm^{-3})	$\Delta[H]$(cm^{-3})
−1.2	1×10^{17}	2.0×10^{17}	1×10^{17}
−4.5	1×10^{18}	1.6×10^{18}	6×10^{17}
−16.5	7×10^{18}	1.0×10^{19}	3×10^{18}

TABLE III. Simulated density of states parameters for the spectra of a-IGZO TFTs with varying concentrations of hydrogen. Max DoS amplitudes are fixed according to the values determined from the $I_D - V_G$ transfer curve shift. The $[O_O^{2-}H^+]^{1-}$ peak energy is at −2.8 or 0.4 eV above the VBM. E_U is the Urbach energy, the only free parameter needed to simulate the experimental trap density and DoS spectra shown in Fig. 3.

ΔV_{ON} (V)	$[H]_{ID-VG}$ (cm^{-3})	E_U (meV)
0	1×10^{16}	95
−1.2	1×10^{17}	100
−4.5	1×10^{18}	140
−16.5	7×10^{18}	180

established, however, is the energetic location at which the resulting bond state manifests in the a-IGZO subgap. Density functional theory calculations indicate the existence of a possible shallow donor state ∼0.4 eV below the conduction band mobility edge[22] and enhanced state density in hydrogen-rich devices has been reported to be observed in the range of 0.2−0.6 eV below the conduction band mobility edge.[12,32] However, hydrogen incorporation in a-IGZO has also been repeatedly correlated with an increased response from states in the near valence band region of the subgap,[9,11,17,23,28,33] which at least one author[33] has suggested could be linked to OH^--interaction.

More commonly, however, both observed changes in state density near the valence band and various electrical effects such as worsened bias illumination stressing in hydrogen-incorporated devices have been associated with the formation of a hydrogen–oxygen vacancy (or hydrogen–metal) complex.[9,10,22,34] However, hydrogen passivation of oxygen vacancies cannot explain the negative V_{ON} shift because the corresponding hydrogen incorporation defect reaction, i.e., $H^0 + V_O{}^0 \rightarrow [HV_O]^0$, is electrically neutral. Any viable model for hydrogen incorporation in a-IGZO must include a defect reaction in which an electron (or electrons) is one of the products on the right side of the defect reaction, e.g., see Eq. (3), in order to account for hydrogen's donor-like behavior.

The potential existence of molecular hydrogen (H_2) in a-IGZO is an unresolved question because the electrically neutral nature and infrared invisibility of H_2 renders experimentally resolving its presence in semiconductors a generally difficult endeavor.[35,36] While the existence of H_2 in semiconductors was theoretically predicted in 1983, it was not confirmed experimentally until 1996 for GaAs, 1997 for Si, 2006 for Ge, and 2009 for ZnO.[35–40] Previous work on hydrogen in a-IGZO has asserted that H_2 is unstable in a-IGZO as it dissociates upon interaction with oxygen vacancy sites.[9] However, the 74 pm equilibrium interatomic radius of H_2 means that it can readily fit into the nanovoids present in the a-IGZO network. In this work, we explore an alternative process for H_2 interaction with a-IGZO that entails dissociation into a short-lived, unstable neutral hydrogen state ($H^{\#0}$) prior to donating its electron and subsequent incorporation into the a-IGZO network via bonding with valence band oxygen atoms.

TABLE II. Figures of merit extracted from the simulation of the DoS spectra in Fig. 3. The first column identifies our suggested peak assignments as originating from $[O_O^{2-}H^+]^{1-}$ bonds, metal vacancies V_M, oxygen vacancies V_O, or the OH stretching mode. Subsequent columns contain the respective peak energies, peak trap densities, and the FWHM spectral width of each peak.

Peak	E_{Peak} (eV)	Max ($cm^{-3}\,eV^{-1}$)	FWHM (eV)
$[O_O^{2-}H^+]^{1-}$	−2.8	see Table III	0.32
V_M	−2.15	2×10^{15}	0.10
V_O	−1.78	7×10^{16}	0.10
V_O	−1.25	4×10^{16}	0.13
V_O	−0.7	1.5×10^{16}	0.09
$OH_{Vibronic}$	−0.37	1×10^{16}	0.05

There are many reports in the literature in which x-ray photoelectron spectroscopy (XPS) is (assertedly) employed for the assessment of oxygen vacancies and/or hydrogen donors present in bulk a-IGZO. Conclusions from these studies are not viable. Since the atomic sensitivity of XPS is ∼0.1−1 at. % and the atomic density of a-IGZO is 8.2×10^{22} cm^{-3}, the best-case XPS sensitivity for the assessment of a-IGZO is ∼10^{20} cm^{-3}. However, oxygen vacancy or hydrogen donor concentrations in a-IGZO are typically on the order of ∼10^{15}−10^{18} cm^{-3}, multiple orders of magnitude below the detection limit of XPS. The pitfall associated with these erroneous literature claims is that these researchers have deconvolved small oxygen 1s XPS peak features associated with adventitious hydrocarbons or other adsorbed surface species and interpreted (incorrectly) that these surface features correspond to bulk oxygen vacancy and/or hydroxide concentrations.[41,42]

The objective of the work presented herein is to formulate a physical picture of how hydrogen incorporation is accomplished in a-IGZO and how its incorporation affects the electrical properties of an a-IGZO TFT. Electrical and electro-optic characterization establishes that increasing the hydrogen concentration in a-IGZO (i) increases the density of free electrons in the conduction band, thereby shifting the turn-on voltage of the a-IGZO TFT to lower voltages, (ii) increases the density of subgap states centered at 0.4 eV above the valence band mobility edge, and (iii) increases the valence band tail state characteristic (Urbach[43]) energy and, hence, the valence band tail state density. To explain these experimental observations, it is argued that hydrogen acts as an anomalous, non-equilibrium donor in a-IGZO as a consequence of its negative-U property in which the formation of a netural, non-bonded hydrogen is energetically unfavorable.

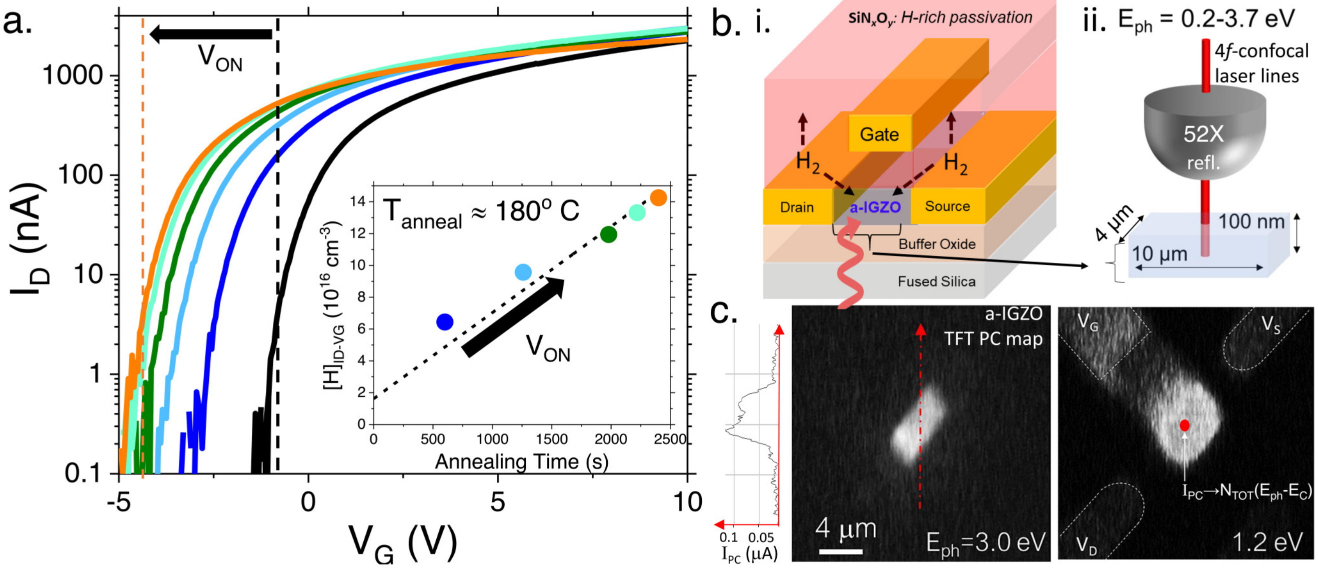

FIG. 1. **(a)** Thermal annealing of a top-gate a-IGZO TFT leads to a negative shift in the drain current–gate voltage (I_D-V_G) transfer curve turn-on voltage (V_{ON}). Each I_D-V_G curve was taken at a different annealing time, represented by the color-coded points in the inset. The value of V_{ON} shifted negatively as a function of annealing time. (Inset) Hydrogen incorporated into a-IGZO as estimated from I_D-V_G transfer curves ($[H]_{ID-VG}$) as a function of annealing time. (b) (i) Cross-sectional view of a typical top-gate a-IGZO TFT measured. When the TFT is thermally annealed at 180 °C, diffusion from the hydrogen-rich SiN_xO_y passivation layer dopes the adjacent a-IGZO active region with hydrogen. **(ii)** The ultrabroadband photoconduction (UBPC) method shown can measure how hydrogen diffusion impacts the total trap density, N_{TOT} by collecting photoconduction current (I_{PC}) for photon excitation energies scanned from E_{ph} = 0.3–3.7 eV. (c) UBPC maps of the collected I_{PC} (see vertical PC-line cut) as a laser raster-scans over a top-gate TFT. Each map results from excitation of a-IGZO subgap traps above $E_{ph} - E_C = -3.0$ or -1.2 eV. N_{TOT} and DoS spectra can then be obtained from the diffraction-limited illumination centered in the active channel (*white arrow*).

II. EXPERIMENTAL METHODS

A. Hydrogen incorporation into a-IGZO top-gate TFTs

To better measure the fundamental properties of hydrogen incorporation in this amorphous semiconductor, a-IGZO TFTs were fabricated in top-gate configuration. Figure 1(bi) shows a cross-sectional view of a top-gate TFT and highlights that the H-rich SiN_xO_y passivation layer is adjacent to the a-IGZO layer active region. Upon controlled thermal annealing, Fig. 1(bi) shows that the top-gate configuration enables facile hydrogen diffusion from the H-rich SiN_xO_y regions directly to the active channel of a-IGZO. Various top-gate TFTs were measured with channel widths ranging from 2.5 to 8 μm and channel lengths between 12 and 16 μm. Unless otherwise noted, measurements presented correspond to TFTs with a 100 nm a-IGZO layer and with channel dimensions shown in Fig. 1(bii). The top-gate insulator capacitance density is 34.5 nFcm^{-2}.

To promote the diffusion of hydrogen from the H-rich passivation layer into the adjacent a-IGZO active channel, the TFT was thermally annealed at 180 °C, leading to a negative shift in the a-IGZO TFT turn-on voltage, V_{ON}, with increasing annealing time. The inferred hydrogen concentration corresponding to the observed negative shift in V_{ON} is estimated as

$$[H]_{ID-VG} = (-C_I V_{ON}/q)^{3/2}, \qquad (1)$$

where $C_I = 34.5$ nF cm^{-2} is the top-gate insulator capacitance density and q is the electronic charge. The drain current–gate voltage curves shown in Fig. 1(a) were measured at the times corresponding to the color-coded points shown in the inset and indicate that the I_D-V_G curve V_{ON} value shifted negatively as a function of annealing time. Using Eq. (1), the inset of Fig. 1(a) plots the calculated $[H]_{ID-VG}$ as a function of annealing time.

B. Ultrabroadband photoconduction and DoS

To better understand how a negative shift in the I_D-V_G curve of an a-IZGO TFT is linked to hydrogen diffusion, the integrated subgap trap density (N_{TOT}) is measured. Direct observation of the subgap trap density has proved difficult in the past[44,45] because the relatively small concentration of traps in the subgap necessitates a roughly 10^{-6} level of precision in order to resolve against background. Ultrabroadband photoconduction (UBPC) is an on-chip microscopy method using highly tunable lasers to resolve the density of subgap traps through precision measurements of TFT photoconductivity (PC). Figure 1(bi) shows the basic elements of UBPC with further details provided in the supplementary material.

Spanning the full IR to UV range, measuring the subgap a-IGZO states uses multiple lasers continuously tunable from 0.3 to 3.7 eV. Specifically, a Coherent Chameleon Ti:Sapphire laser is coupled to an APE Compact optical parametric oscillator and a HarmoniXX second harmonic generation system. To minimize spectral aberrations, we use all-reflective optics, including a 52X high-NA reflective objective. A piezo-scanning mirror within a 4f confocal system couples the laser lines into an Olympus BX61W microscope with a homebuilt transport setup. While the photon energy E_{ph} is scanned step-wise from 0.3 to 3.7 eV, inverted RF source-drain electrical probes collect the PC induced by the laser (I_{PC}). I_{PC} is detected by an current pre-amplifier and a lock-in amplifier (Zurich HFLI) referenced to an optical chopper frequency modulating the laser at 585 Hz. Dark-curve background and illuminated transfer curve hysteretic drift is removed from the I_{PC} signal by careful selection of the lock-in amplifier laser-chopping frequency.

Figure 1(c) shows PC-maps generated by raster-scanning the laser at E_{ph} over a top-gate a-IGZO TFT. It produces a spatially uniform I_{PC} response over the a-IGZO TFT active region. Precision scanning optics maintain a diffraction-limited spot at the a-IGZO TFT center for the duration of UBPC measurement. The I_{PC} signal must be normalized by the number of photons incident per second on the active region, N_{ph}. To accomplish this, both the laser power transmitted through the objective and through-objective+TFT chip are measured at each photon energy. The resulting measured signal, qI_{PC}/N_{ph}, is directly proportional to the total integrated trap density, N_{TOT}, from the conduction band mobility edge to the photon energy, E_{ph}, according to

$$N_{TOT}(E_{ph}) = \left(\frac{I_{PC}}{N_{ph}}\right)\left(\frac{qC_I}{m}\right)\frac{N_{o,max}}{d}, \tag{2}$$

where d is the thickness of a-IGZO, and m is the slope of the dark $I_D - V_G$ transfer curve in the linear region within ± 0.5 V of the constant 5 V forward gate bias voltage over which the UBPC signal, I_{PC} was collected. $N_{o,max}$ is a constant calibration factor obtained by finding the maximum number of incident photons per second that give a measurable increase in the PC-response, i.e., the saturation photon flux measured at the near-bandgap. Note that the notation $E - E_C = -E_{ph}$ is used interchangeably.

Finally, the a-IGZO experimental density of states (DoS) is obtained by taking a derivative of the total subgap trap density or $\mathrm{DoS}(E_{ph}) = \frac{dN_{TOT}}{dE_{ph}}$. For the as-grown a-IGZO TFTs, the experimental DoS peaks were simulated as Gaussian peaks and exponential Urbach tails. Then, using the $[H]_{ID-VG}$ values obtained from $I_D - V_G$ transfer curve measurements and the Tauc[46–48] bandgap analysis (see supplementary material), a simulated hydrogen-dependent DoS is compared again with the experimental curve.

III. EXPERIMENTAL RESULTS AND DISCUSSION

Figure 2(a) shows $I_D - V_G$ curves for four top-gate a-IGZO TFTs possessing varying concentrations of hydrogen (see Sec. II A for an explanation of how hydrogen is introduced into the a-IGZO TFT channel layer). A higher concentration of hydrogen corresponds to a more negative turn-on voltage, V_{ON}, indicating that incorporated hydrogen is electrically active and that hydrogen behaves as a donor dopant since it increases the density of free conduction band electrons within the a-IGZO channel layer, thereby shifting V_{ON} to a more negative voltage.

Figure 2(b) presents Tauc photoconductance plots for four top-gate a-IGZO TFTs possessing varying concentrations of hydrogen. Details of the Tauc scaling of the UBPC photoconduction data are provided in the supplementary materials. The optical bandgap is estimated via a linear regression fitting of the valence band onset portion of the Tauc plot, yielding a bandgap of $E_g = 3.17$ eV for a-IGZO prior to hydrogen incorporation. While the bandgap does not change appreciably with hydrogen incorporation (averaging to 3.15 ± 0.04 eV over the four devices), the Tauc plot in the subgap region increases with increasing hydrogen concentration for subgap states positioned within ∼0.4 eV of the valence band mobility edge. Thus, Tauc photoconductance plots indicate that increasing hydrogen concentration increases the density of subgap electronic states located within ∼0.4 eV above the valence band mobility edge.

Figure 2(c) shows the total integrated trap density, N_{TOT} (cm^{-3}), for four top-gate a-IGZO TFTs possessing varying concentrations of hydrogen. N_{TOT} is evaluated via ultrabroadband photoconduction (UBPC) as described in Sec. II B. While N_{TOT} increases monotonically with increasing hydrogen concentration, this increase occurs almost exclusively in the near-valence band portion of the bandgap. In the upper portions of the bandgap, from ~ -2 to -0.5 eV, the N_{TOT} signal originates from mainly the photoionization of oxygen vacancy-related subgap traps and is independent of the incorporated hydrogen concentration. Thus, the UBPC data demonstrate that hydrogen incorporation into a-IGZO gives rise to the creation of subgap electronic states located in the lower portion of the bandgap.

The inset of Fig. 2(c) offers another perspective on hydrogen-induced subgap trap creation using UBPC trap density difference curves, obtained by taking $\Delta N_{TOT}(V_{ON}) = N_{TOT}(V_{ON}) - N_{TOT}(V_{ON} = 0\,\mathrm{V})$. As before, an increase in trap density near the valence band mobility edge occurs as hydrogen incorporation increases. The logarithmic ordinate scale employed in Fig. 2(c) uses a seven orders of magnitude scale to explore the subtle density of states features associated with the high dynamic range of UBPC. Comparison against the linear ordinate scaling shown in Fig. S4 in the supplementary material is helpful to emphasize that hydrogen-induced subgap state creation primarily occurs within ∼0.4 eV of the valence band mobility edge.

How much hydrogen is incorporated into the four a-IGZO TFTs under consideration? Two methods are employed to estimate the incorporated hydrogen concentration. From $I_D - V_G$ transfer curves [Fig. 2(a)], the incorporated hydrogen is estimated using $[H]_{ID-VG} = (-C_I V_{ON}/q)^{3/2}$ where $C_I = 34.5\,\mathrm{nF\,cm^{-2}}$ is the gate insulator capacitance density and q is electronic charge. From differential trap density measurement, the incorporated hydrogen concentration is estimated using $[H]_{UBPC} = \Delta N_{TOT}(E = E_g \cong -3.2)$ eV. The inset of Fig. 2(c) shows that the $[H]_{I_D-V_G}$ (horizontal lines) are indeed very similar to the UBPC ΔN_{TOT} measurements taken at the intercept to the E_g vertical dashed line.

While Table I shows that the hydrogen concentrations estimated from $I_D - V_G$ transfer curves and UBPC are similar, $[H]_{UBPC}$ is always found to be larger than $[H]_{ID-VG}$, by a factor of ~ 2. This suggests that hydrogen incorporation in a-IGZO leads to the creation of two types of electronic subgap states. First, hydrogen

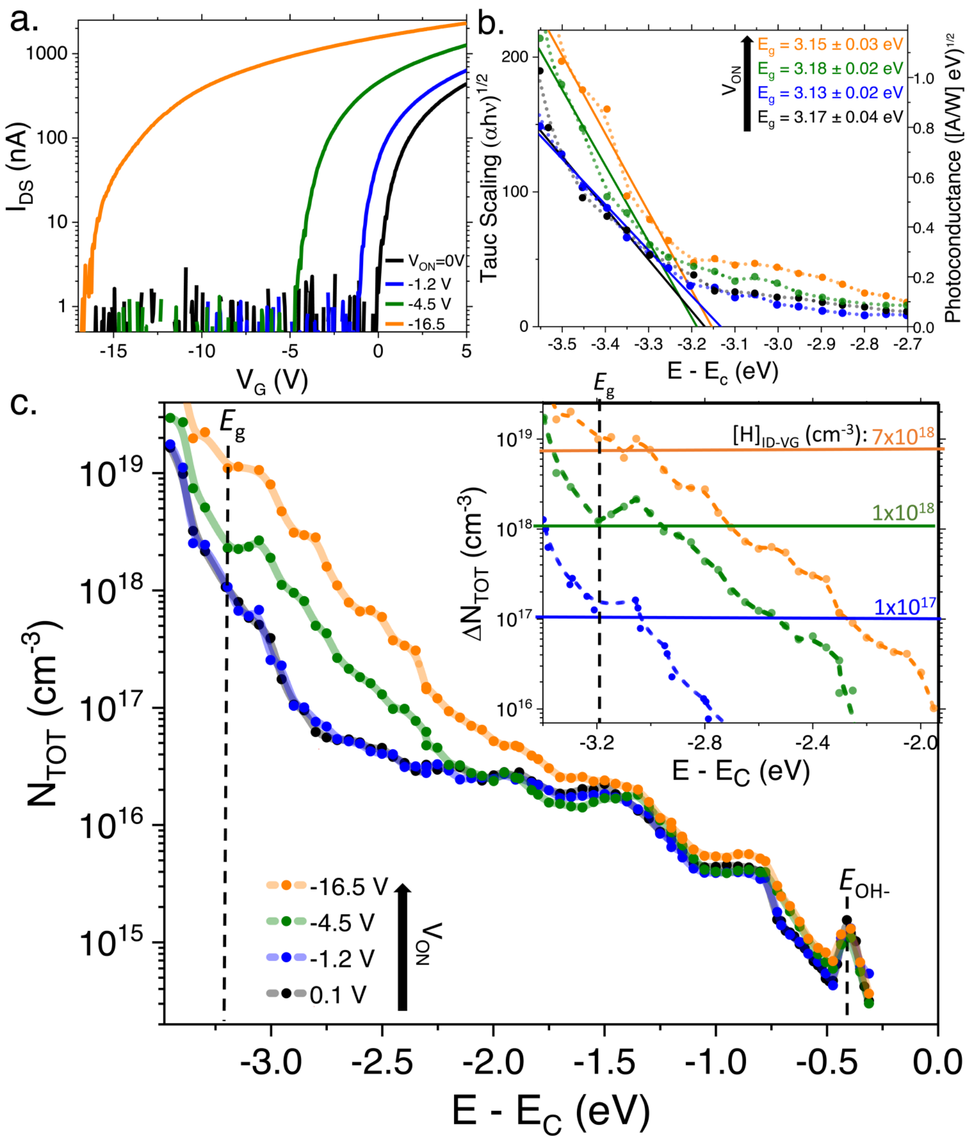

FIG. 2. (a) Drain current–gate voltage (I_D-V_G) transfer curves for four top-gate a-IGZO TFTs with varying levels of hydrogen incorporation; a larger hydrogen concentration in the a-IGZO channel layer corresponds to a more negative shift in the turn-on voltage. (b) The UBPC photoconduction signal estimates the bandgap of top-gate a-IGZO TFTs. For four different V_{ON} device conditions, the Tauc plot scaling linear fits are shown (solid lines). The bandgap for the pre-hydrogen incorporation a-IGZO TFT is ~3.17 ± 0.04 eV. (c) The UBPC total integrated trap density, N_{TOT}, is plotted from 0.3 eV below the conduction band to the valence band region. (Inset) Plot of the differential or background-subtracted (V_{ON} = 0 V curve) trap density maximizes the contribution from subgap states that contribute to each observed I_D-V_G V_{ON} shift. The colored dashed lines correspond to the hydrogen concentration calculated directly from I_D-V_G transfer curves. At the valence band mobility edge (E_g, vertical line), these I_D-V_G estimates are similar to the UBPC trap density measurement value.

donor states ($[H]_{ID-VG}$) are electrically active and form a Gaussian-like band centered at ~ 0.4 eV above the valence band mobility edge. Second, hydrogen-induced valence band tail states ($[H]_{UBPC} - [H]_{ID-VG}$) constitute an enhancement of the valence band tail state density (and, hence, the valence band Urbach energy, W_{TD}) due to the incorporation of hydrogen [which increased disorder on the anion (oxygen) sublattice]; since valence band tail states are donor-like, they are electrically neutral and, hence, electrically inactive from the perspective of a-IGZO TFT operation.

Figure 3 shows a comparison between the experimental subgap density of states (DoS) of the four a-IGZO TFTs from the N_{TOT} UBPC measurement. The solid lines are simulations based on a Gaussian hydrogen donor subgap peak centered at −2.8 eV convolved with an Urbach[6,43] tail whose characteristic energy increases monotonically with hydrogen concentration due to increased disorder of the anion sublattice from which the valence band tail states originate. The simulation reproduces both the experimental density of states and trap density (shown in the inset of Fig. 3). Based on the simulation and experimental data, the composition of the a-IGZO subgap is quantified in Table II. The simulated peak maximum values and Urbach tail energies corresponding to the density of states spectra for the a-IGZO TFTs of varying hydrogen levels shown in Fig. 3 are provided in Table III. The simulation response is dominated by the −2.8 eV peak whose density was fixed to that of the $[H]_{ID-VG}$ values. As such, the Urbach energy, E_U in Table III, is the only free parameter required to match the simulation to the experiment.

IV. DISCUSSION: HYDROGEN IN a-IGZO

$[H]_{ID-VG}$ in Table I is an estimate of the electrically-active hydrogen incorporated into a-IGZO that gives rise to a corresponding increase in the subgap state density just above the valence band mobility edge. Since valence band states are derived primarily from O 2p atomic orbital basis states, it is clear that incorporated hydrogen mainly interacts with the oxygen anion sublattice, as described by the defect reaction

$$O_O^{2-} + H^0 \rightarrow [\ O_O^{2-}H^+\ ]^{1-} + e^-, \tag{3}$$

where O_O^{2-} denotes a bonded oxygen ion sitting on an oxygen site that is embedded within the a-IGZO amorphous network, presuming an ionic bonding model such that the oxygen ion is assumed to possess a 2− charge state, H^0 is a neutral hydrogen atom being incorporated into the a-IGZO network, $[O_O^{2-}H^+]^{1-}$ is a defect complex consisting of a bonded O_O^{2-} oxygen interacting coulombically (primarily) with a positively ionized hydrogen atom such that an overall charge state of 1− exists for this defect complex (it is possible to more simply and equivalently identify this defect complex as OH^- but we prefer to use the $[O_O^{2-}H^+]^{1-}$ notation as it more accurately captures the detailed nature of the interaction (bonding) between oxygen and hydrogen), and e^- is a free conduction band electron giving rise to the negative turn-on voltage shift witnessed in Fig. 2(a). Note that the presence of free electrons on the right side of Eq. (3) defect reaction is consistent with hydrogen behaving as a donor.

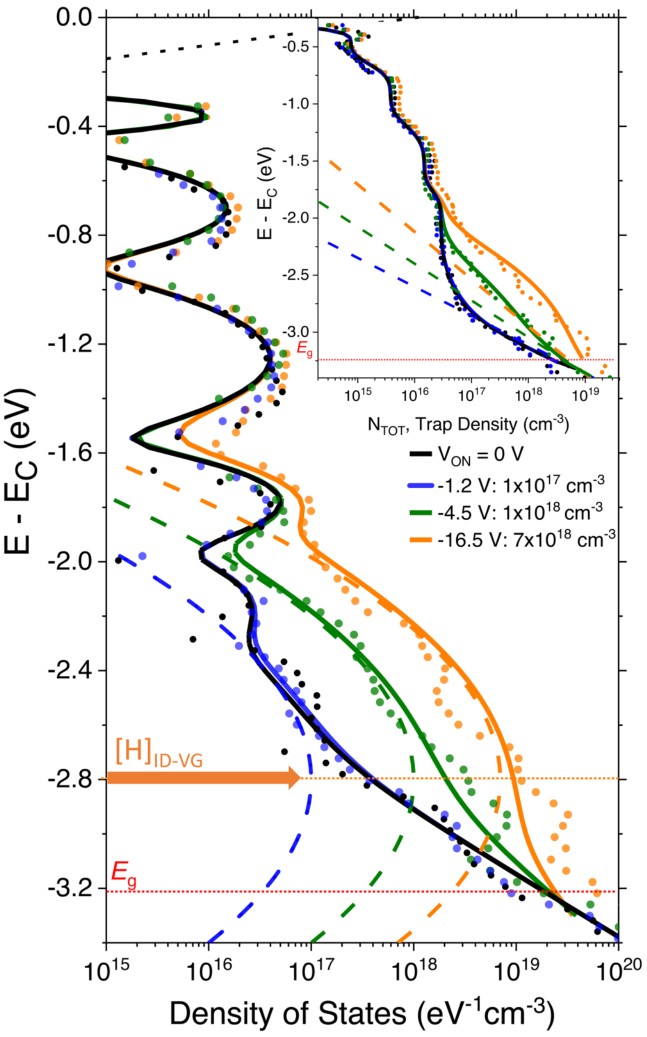

FIG. 3. Plot of the experimental (*closed circles*) subgap DoS of top-gate a-IGZO TFTs with varying degrees of hydrogen incorporation. Overlaid is a simulation (*solid lines*) of the convolved subgap defect peaks and the valence band Urbach tail. The Gaussian peak centered (*dashed lines*) at −2.8 eV is most salient for the $V_{ON} = -4.5$ and −16.5 V shifted curves, and its simulated peak density was constrained to be equal to the $[H]_{ID-VG}$ trap density. After all peaks of the $V_{ON} = 0$ V case were simulated, the Urbach tail energy was the only free simulation parameter (95−180 meV). ***(Inset)*** The corresponding experimental total integrated trap density (*closed circles*) and the integral of the simulated DoS (*solid lines*) confirm the DoS simulation predicts the UBPC trap density hydrogen dependence. *Dashed lines* are the simulated change in valence band Urbach energy.

Isolating the hydrogen portion of the defect reaction discussed above, i.e., $H^0 \rightarrow H^+ + e^-$, demonstrates that hydrogen incorporation involves donor ionization, where hydrogen is the donor. This observation leads to the following question: How is it possible for donor ionization to occur from subgap states residing just above the valence band mobility edge? Clearly, donor ionization cannot be accomplished in the normal manner, i.e., by thermal emission of a neutral donor electron to the conduction band, since the H-induced subgap states are located ∼2.8 eV below the conduction band mobility edge. As discussed below, understanding donor ionization in the context of hydrogen incorporation requires the elucidation of the negative-U character of hydrogen.[38,49]

Figure 4(a) illustrates in a generic, idealized sense the formation energy as a function of Fermi-level position trend for hydrogen residing within a semiconductor or insulator solid *assuming* that hydrogen behaves as a positive-U defect (which it does *not*; U denotes correlation energy, as discussed below). Three charge states are possible for hydrogen, i.e., neutral (H^0), positively ionized (H^+), or negatively ionized (H^-). The trend according to Fig. 4(a) is that H^+ is energetically preferred when the Fermi level is located near the valence band, while H^- has the lowest formation energy when the Fermi level is close to the conduction band; H^0 is energetically favorable when the Fermi level is near midgap. The type of defect behavior shown in Fig. 4(a) results in two distinct ionization energies in which (i) a positive charge state transitions to a neutral charge state (donor neutralization) and (ii) a neutral charge state transitions to a negative charge state (acceptor ionization) as the Fermi level is modulated across the bandgap from the valence band to the conduction band mobility edge. Notice that each charge state transition shown in Fig. 4(a) involves only one electron. This type of formation energy-Fermi level trend is often classified as "normal" since it is typically expected that a charge state transition involves only one electron. Classifying positive-U as "normal" is not advisable, however, since Robertson and co-workers have

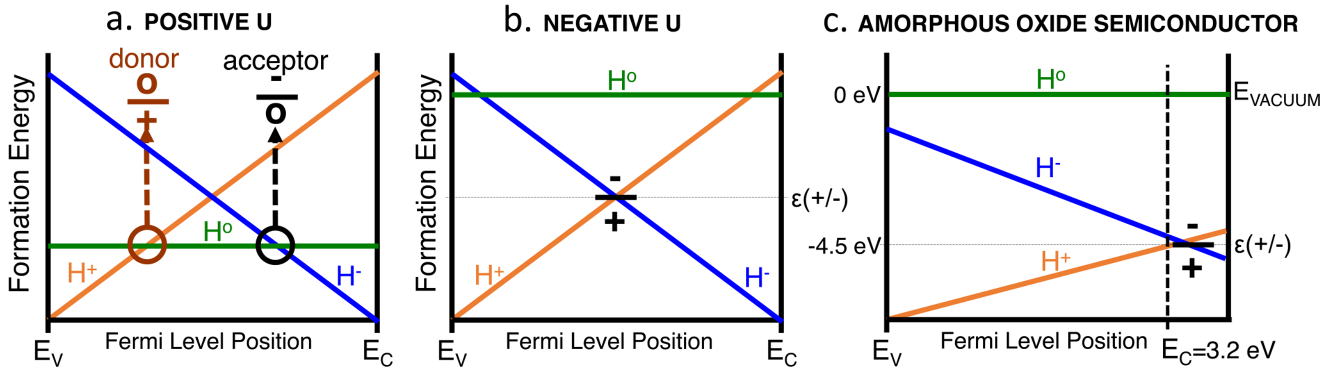

FIG. 4. (a) Positive U and (b) negative U formation energy vs Fermi level position trends for hydrogen incorporation into a generic semiconductor or insulator. In contrast, (c) displays the expected Fermi-level position trend for hydrogen incorporation into an amorphous oxide semiconductor such as a-IGZO ($E_g \sim 3.2$ eV), with the ordinate corresponding to the energies referenced to the vacuum level.

discovered that negative-U is the common or "normal" case for hydrogen in wide-bandgap oxides.[50–52]

In contrast, Fig. 4(b) exhibits a different type of formation energy as a function of Fermi level position trend as a consequence of a re-positioning of the neutral H^0 formation energy (which does not depend on the Fermi level) to a higher energy than that shown in Fig. 4(a). This leads to a situation in which only one ionization energy exists, and any charge state transition involves two electrons. For our purposes, negative-U behavior of hydrogen in a solid corresponds to a situation as shown in Fig. 4(b), in which the neutral H^0 formation energy is always larger than that of the H^+ or H^- formation energy, depending on where the Fermi level is positioned. Quantitatively, if we define correlation energy as $U = E_F(0/-) - E_F(+/0)$ (other definitions for correlation energy are possible), then the positive- or negative-U nature of hydrogen in a solid is clear and unambiguous.

Figures 4(a) and 4(b) are generic, idealized examples of positive-U and negative-U trends for hydrogen in a semiconductor or insulator solid. Figure 4(c) is a more realistic version of what the formation energy-Fermi level position might look like for an amorphous oxide semiconductor such as a-IGZO. [Fig. 4(c) is similar to that shown for Ga_2O_3 in Fig. 11 of Ref. 44.] Three aspects of Fig. 4(c) are important. First, hydrogen is a negative-U defect in a-IGZO. Second, the +/− ionization energy for a-IGZO is likely degenerate with the conduction band, rather than in the middle of the bandgap as shown in Figs. 4(a) and 4(b). This means that the H^+ charge state is more likely to exist in a-IGZO than the H^- charge state. Third, the ordinate of Fig. 4(c) has been changed to illustrate how it might look with respect to the vacuum level, in accordance with the universal alignment of hydrogen theory of Van de Walle and Neugebauer,[38,49] while the neutral hydrogen formation energy is positioned at the vacuum level.

Energy positioning of the hydrogen +/− energy and H^0 merits a bit more clarification. Van de Walle and Neugebauer assert that the hydrogen +/− ionization energy is invariably positioned at or near −4.5 eV from the vacuum level for all semiconductors, insulators, and even for aqueous solutions, and that this universal positioning corresponds to the standard hydrogen electrode potential of electrochemistry.[38,49] Note that the bond dissociation energy of molecular hydrogen, H_2, is 435.7 kJ/mol or 4.5 eV. Thus, when molecular hydrogen is present in a-IGZO, it is energetically positioned at −4.5 eV below the vacuum level, corresponding to its potential or bond dissociation energy. If H_2 dissociates into two neutral atoms, $2H^0$, within the a-IGZO network, these neutral hydrogen atoms are neither bonded to the a-IGZO lattice nor to themselves such that they only possess a small amount of kinetic energy and are positioned slightly above the vacuum level, as shown in Fig. 4(c).

Energetic positioning of neutral hydrogen in a-IGZO at or near the vacuum level is likely confusing to many readers since it is well-known that the ground-state ionization energy of hydrogen is −13.6 eV. The hydrogen ground state is indeed positioned at −13.6 eV below the vacuum level for hydrogen in the gas phase. However, in our case, hydrogen is confined within an a-IGZO network. Using a simple atomic confinement model consisting of a hydrogen atom constrained to a spherical box, it is found that for a box diameter less than 196 pm, the hydrogen atom is no longer bound because its 1s energy is positive, while a box diameter greater than 500 pm ensures that the 1s energy is close to that of gas-phase hydrogen, i.e., −13.6 eV.[53,54] Thus, nanovoids present in a-IGZO likely result in strong confinement of neutral hydrogen, but these nanovoids are not simple spheres and have variable effective diameters, and it is unclear whether they are best modeled using soft- or hard-confinement barriers.[55] In summary, we picture neutral atomic hydrogen in a-IGZO as a short-lived, metastable specie whose energy fluctuates at or near the vacuum level as it moves (possibly via tunneling) within the a-IGZO network.

Finally, after this extended negative-U behavior detour, we are now in an excellent position to answer the previously posed question: How is it possible for donor ionization to occur from subgap states residing just above the valence band mobility edge? The answer is that hydrogen donors behave differently from other donors. Most donors are first embedded into the lattice network, after which donor ionization occurs. In contrast, donor ionization occurs when hydrogen is in its neutral charge state, prior to its incorporation into the lattice. After ionization, hydrogen is incorporated into the network as a positively charged species. Since H^0

is positioned at or near the vacuum level, no donor ionization energy barrier exists for hydrogen and the energetic positioning of its subgap states is irrelevant.

Figure 5 presents a comparison between a normal donor and a hydrogen donor. As evident from an assessment of Fig. 5, hydrogen donor behavior is significantly different from that of normal donor behavior. When a normal donor (D, indicated as red in Fig. 5) is incorporated into a lattice, it creates a neutral subgap state that is easily thermally ionized, sending its electron into the conduction band. The important point here is the behavioral sequence of a normal donor, involving *neutral* incorporation → subgap state creation → ionization. In contrast, the behavioral sequence for a hydrogen donor (H, indicated as blue in Fig. 5) is distinctly different, involving ionization → *ionized* incorporation → subgap state creation. More specifically, hydrogen is initially present in the lattice as neutral, non-bonded hydrogen, H^0, confined interstitially within the network. Non-bonded H^0 is energetically unstable (metastable) such that it rapidly ionizes to H^+ with the ionized electron thermalizing to the bottom of the conduction band [Fig. 5(a)]. (If interstitial, non-bonded molecular hydrogen is envisaged is the original source of hydrogen to be incorporated into the lattice, then neutral, non-bonded hydrogen essentially acts as an activated complex facilitating hydrogen ionization, i.e., $\frac{1}{2}H_2 \rightarrow H^{\#0} \rightarrow H^+ + e^-$, where the symbol # is used to denote an activated complex.) The charged nature of H^+ provides a Coulombic driving force for it to bond to an oxygen-on-an-oxygen-site valence band state, O_O^{2-}, thereby incorporating itself into the lattice via the formation of an $[O_O^{2-}H^+]^{1-}$ defect complex and creating an associated subgap state energetically positioned just above the valence band mobility edge. Notice that the formation of the $[O_O^{2-}H^+]^{1-}$ defect complex involves energetic re-positioning of the O_O^{2-} valence band state from below to above the valence band mobility edge due to its complexing with H^+ [Fig. 5(b)].

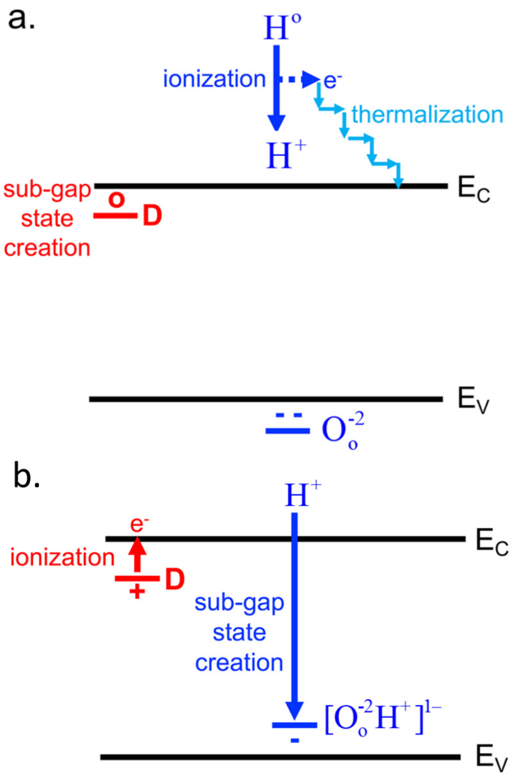

FIG. 5. Normal donor vs hydrogen donor behavior. (a) A normal donor (D, *red*) creates a neutral, subgap state just below the conduction band minimum when it is incorporated into the lattice and then in (b-*red*) is positively ionized by thermal emission of an electron into the conduction band. In contrast, hydrogen (H, *blue*) is initially present in the lattice as neutral, non-bonded hydrogen (H^0). Then, in (a-*blue*), H^0 ionizes to H^+ with the ionized electron thermalizing to the bottom of the conduction band. Finally, in (b-*blue*) H^+ is incorporated into the lattice, thereby creating (in an oxide) a subgap state just above the valence band mobility edge due to the formation of an $[O_O^{2-}H^+]^{1-}$ defect complex in which an oxygen-on-an-oxygen-site valence band state O_O^{2-} is pushed into the bandgap due to forming a complex with H^+.

In summary, the key difference here is that for a normal donor, subgap state creation occurs first, followed by ionization. In contrast, for the unusual case of a hydrogen donor, ionization occurs first, followed by subgap state creation. Normal donor ionization is controlled by the position of the Fermi level with respect to the donor ionization energy and is, thus, an equilibrium thermodynamic process. In contrast, since hydrogen donor ionization occurs prior to incorporation into the lattice when subgap states are created, hydrogen donors always remain ionized, independently of the position of the Fermi level; hence, hydrogen donor ionization is a non-equilibrium phenomenon.

V. CONCLUSIONS

The chemistry and physics of hydrogen incorporation into an a-IGZO TFT channel layer are quite subtle. Experimentally, hydrogen behaves as a donor since its incorporation leads to a negative shift in the TFT turn-on voltage due to an increase in the concentration of free conduction band electrons. However, hydrogen is clearly not a simple donor since its incorporation results in the creation of a Gaussian distribution of subgap electronic states centered at 0.4 eV above the valence band mobility edge and also in an enhancement of the valence band tail state density as witnessed by an increase in the valence band Urbach energy. The hydrogen-induced, Gaussian-distributed, donor-like subgap electronic states arise as a consequence of the negative-U behavior of hydrogen in a-IGZO in which hydrogen ionization precedes its incorporation into the lattice network, resulting in the formation of a $[O_O^{2-}H^+]^{1-}$ defect complex. Furthermore, the formation of a $[O_O^{2-}H^+]^{1-}$ defect complex or equivalently of an OH- bond leads to positional distortion of the oxygen ion, thus increasing the amount of disorder existing on the anion sublattice and increasing the valence band tail state density. The charge state of these hydrogen-induced subgap and band tail states are controlled by non-equilibrium and equilibrium thermodynamics, respectively, since they exist in their most positive and neutral charge states, respectively, when the Fermi level is located near to the conduction band mobility edge.

Although a detailed explication of hydrogen incorporation into a-IGZO has been presented, a key question remains unanswered: Why is the concentration of electrically active hydrogen orders of magnitude smaller than the total concentration of hydrogen as estimated from SIMS analysis? Presumably most of this SIMS-measured hydrogen exists as molecular hydrogen, H_2. Moreover, it is likely that H_2 is a precursor for electrically-active hydrogen incorporation. But why should such a tiny fraction of this molecular hydrogen become electrically active and what controls this? Answering these questions requires further investigation.

SUPPLEMENTARY MATERIAL

See the supplementary material for further method details and UBPC datasets with a power-dependent analysis.

AUTHOR DECLARATIONS

Conflict of Interest

The authors declare no conflict of interest.

DATA AVAILABILITY

The data that support the findings of this study are available from the corresponding author upon reasonable request.

REFERENCES

[1] K. Nomura, H. Ohta, A. Takagi, T. Kamiya, M. Hirano, and H. Hosono, Nature **432**, 488 (2004).

[2] T. Kamiya, K. Nomura, and H. Hosono, Sci. Technol. Adv. Mater. **11**, 044305 (2010).

[3] J. Y. Kwon, D. J. Lee, and K. B. Kim, Electron. Mater. Lett. **7**, 1 (2011).

[4] J. F. Wager, Inf. Disp. **36**, 9 (2020).

[5] K. T. Vogt, C. E. Malmberg, J. C. Buchanan, G. W. Mattson, G. M. Brandt, D. B. Fast, P. H.-Y. Cheong, J. F. Wager, and M. W. Graham, Phys. Rev. Res. **2**, 033358 (2020).

[6] J. F. Wager, AIP Adv. **7**, 125321 (2017).

[7] J. Lee, J.-S. Park, Y. S. Pyo, D. B. Lee, E. H. Kim, D. Stryakhilev, T. W. Kim, D. U. Jin, and Y.-G. Mo, Appl. Phys. Lett. **95**, 123502 (2009).

[8] T. Miyase, K. Watanabe, I. Sakaguchi, N. Ohashi, K. Domen, K. Nomura, H. Hiramatsu, H. Kumomi, H. Hosono, and T. Kamiya, ECS J. Solid State Sci. Technol. **3**, Q3085 (2014).

[9] J. Bang, S. Matsuishi, and H. Hosono, Appl. Phys. Lett. **110**, 232105 (2017).

[10] H. Li, Y. Guo, and J. Robertson, Sci. Rep. **7**, 1 (2017).

[11] A. Song, H.-W. Park, K.-B. Chung, Y. S. Rim, K. S. Son, J. H. Lim, and H. Y. Chu, Appl. Phys. Lett. **111**, 243507 (2017).

[12] K.-L. Han, K.-C. Ok, H.-S. Cho, S. Oh, and J.-S. Park, Appl. Phys. Lett. **111**, 063502 (2017).

[13] A. Abliz, Q. Gao, D. Wan, X. Liu, L. Xu, C. Liu, C. Jiang, X. Li, H. Chen, T. Guo, J. Li, and L. Liao, ACS Appl. Mater. Interfaces **9**, 10798 (2017).

[14] Y. Nam, H. O. Kim, S. H. Cho, and S. H. Ko Park, RSC Adv. **8**, 5622 (2018).

[15] J. C. Felizco, M. Uenuma, Y. Ishikawa, and Y. Uraoka, Appl. Surf. Sci. **527**, 146791 (2020).

[16] H.-C. Chen, J.-J. Chen, K.-J. Zhou, G.-F. Chen, C.-W. Kuo, Y.-S. Shih, W.-C. Su, C.-C. Yang, H.-C. Huang, C.-C. Shih, W.-C. Lai, and T.-C. Chang, IEEE Trans. Electron Devices **67**, 3123 (2020).

[17] X.-L. Wang, Y. Shao, X. Wu, M.-N. Zhang, L. Li, W.-J. Liu, D. W. Zhang, and S.-J. Ding, RSC Adv. **10**, 3572 (2020).

[18] A. Abliz, J. Alloys Compd. **831**, 154694 (2020).

[19] D. C. Corsino, J. P. S. Bermundo, M. N. Fujii, K. Takahashi, Y. Ishikawa, and Y. Uraoka, J. Phys. D: Appl. Phys. **53**, 165103 (2020).

[20] O. K. Prasad, S. K. Mohanty, C. H. Wu, T. Y. Yu, and K. M. Chang, Nanotechnology **32**, 395203 (2021).

[21] Y. Magari and M. Furura, Jpn. J. Appl. Phys. **60**, SBBM04 (2021).

[22] A. De Jamblinne De Meux, G. Pourtois, J. Genoe, and P. Heremans, Phys. Rev. Appl. **9**, 54039 (2018).

[23] Y. Lee, T. Nam, S. Seo, H. Yoon, I.-K. Oh, C. H. Lee, H. Yoo, H. J. Kim, W. Choi, S. Im, J. Y. Yang, D. W. Choi, C. Yoo, H. jin Kim, and H. Kim, ACS Appl. Mater. Interfaces **13**, 20349 (2021).

[24] S.-G. Jeong, H.-J. Jeong, W.-H. Choi, K. Kim, and J.-S. Park, IEEE Trans. Electron Devices **67**, 4250 (2020).

[25] H.-C. Chen, J.-J. Chen, Y.-F. Tu, K.-J. Zhou, C.-W. Kuo, W.-C. Su, Y.-H. Hung, Y.-S. Shih, H.-C. Huang, T.-M. Tsai, J.-W. Huang, W.-C. Lai, and T.-C. Chang, IEEE Trans. Electron Devices **67**, 2807 (2020).

[26] C. Liu, H. Qin, Y. Liu, S. Wei, H. Wang, and Y. Zhao, Mater. Sci. Semicond. Process. **121**, 105390 (2021).

[27] H. J. Kim, S. Y. Park, H. Y. Jung, B. G. Son, C.-K. Lee, C.-K. Lee, J. H. Jeong, Y.-G. Mo, K. S. Son, M. K. Ryu, S. Lee, and J. K. Jeong, J. Phys. D: Appl. Phys. **46**, 055104 (2012).

[28] D.-G. Kim, J.-U. Kim, J.-S. Lee, K.-S. Park, Y.-G. Chang, M.-H. Kim, and D.-K. Choi, RSC Adv. **9**, 20865 (2019).

[29] A. Song, H. M. Hong, K. S. Son, J. H. Lim, and K.-B. Chung, IEEE Trans. Electron Devices **68**, 2723 (2021).

[30] H. Kumomi, S. Yaginuma, H. Omura, A. Goyal, A. Sato, M. Watanabe, M. Shimada, N. Kaji, K. Takahashi, M. Ofuji, T. Watanabe, N. Itagaki, H. Shimizu, K. Abe, Y. Tateishi, H. Yabuta, T. Iwasaki, R. Hayashi, T. Aiba, and M. Sano, J. Disp. Technol. **5**, 531 (2009).

[31] K. Nomura, T. Kamiya, and H. Hosono, ECS J. Solid State Sci. Technol. **2**, P5 (2013).

[32] J. T. Jang, D. Ko, S.-J. Choi, D. M. Kim, and D. H. Kim, IEEE Electron Device Lett. **42**, 708 (2021).

[33] B. H. Kang, W.-G. Kim, J. Chung, J. H. Lee, and H. J. Kim, ACS Appl. Mater. Interfaces **10**, 7223 (2018).

[34] K. M. Kojima, M. Hiraishi, H. Okabe, A. Koda, R. Kadono, K. Ide, S. Matsuishi, H. Kumomi, T. Kamiya, and H. Hosono, Appl. Phys. Lett. **115**, 122104 (2019).

[35] J. Weber, M. Hiller, and E. V. Lavrov, Physica B **401–402**, 91 (2007).

[36] S. G. Koch, E. V. Lavrov, and J. Weber, Phys. Rev. B **90**, 205212 (2014).

[37] E. E. Chen, M. Stavola, W. B. Fowler, and P. Walters, Phys. Rev. Lett. **88**, 105507 (2002).

[38] C. G. V. de Walle and J. Neugebauer, Annu. Rev. Mater. Res. **36**, 179 (2006).

[39] M. D. McCluskey and S. J. Jokela, J. Appl. Phys. **106**, 071101 (2009).

[40] E. V. Lavrov, F. Herklotz, and J. Weber, Phys. Rev. Lett. **102**, 185502 (2009).

[41] J. S. Rajachidambaram, S. Sanghavi, P. Nachimuthu, V. Shutthanandan, T. Varga, B. Flynn, S. Thevuthasan, and G. S. Herman, J. Mater. Res. **27**, 2309 (2012).

[42] X. Du, B. T. Flynn, J. R. Motley, W. F. Stickle, H. Bluhm, and G. S. Herman, ECS J. Solid State Sci. Technol. **3**, Q3045 (2014).

[43] F. Urbach, Phys. Rev. **92**, 1324 (1953).

[44] J. T. Jang, J. Park, B. D. Ahn, D. M. Kim, S. J. Choi, H. S. Kim, and D. H. Kim, ACS Appl. Mater. Interfaces **7**, 15570 (2015).

[45] J. Jia, A. Suko, Y. Shigesato, T. Okajima, K. Inoue, and H. Hosomi, Phys. Rev. Appl. **9**, 14018 (2018).

[46] J. Tauc, Mater. Res. Bull. **3**, 37 (1968).

[47] C.-M. Hsu, W.-C. Tzou, C.-F. Yang, and Y.-J. Liou, Materials **8**, 2769 (2015).

[48] W.-S. Liu, C.-L. Huang, Y.-H. Lin, C.-H. Hsu, and Y.-M. Chu, Semicond. Sci. Technol. **35**, 025004 (2019).

[49] C. G. V. de Walle and J. Neugebauer, Nature **423**, 626 (2003).

[50] J. Robertson and P. Peacock, Thin Solid Films **445**, 155 (2003).

[51] K. Xiong, J. Robertson, and S. J. Clark, J. Appl. Phys. **102**, 083710 (2007).

[52] H. Li and J. Robertson, J. Appl. Phys. **115**, 203708 (2014).

[53] N. Aquino, G. Campoy, and H. E. Montgomery, Int. J. Quantum Chem. **107**, 1548 (2007).

[54] C. Laughlin, B. L. Burrows, and M. Cohen, J. Phys. B: At. Mol. Opt. Phys. **35**, 701 (2002).

[55] *Electronic Structure of Quantum Confined Atoms and Molecules*, edited by K. Sen (Springer International Publishing, 2014).